nature communications

Article

https://doi.org/10.1038/s41467-026-74096-8

Charge-spin dichotomy in the kagome metal $CsCr_3Sb_5$

Received: 1 October 2025

Accepted: 19 May 2026

Published online: 17 July 2026

Check for updates

Asato Onishi[1] ✉, Yoichi Kageyama[1,7], Cédric Bareille[2], Sogen Ikegami[1,8], Zifan Xu[1], Kota Ishihara[1], Hirokazu Fujiwara[1,3], Zehao Wang[4,5], Bin Gao[4,5], Weiliang Yao[4,5], Pengcheng Dai[4,5], Youichi Yamakawa[6], Hiroshi Kontani[6], Toshiyuki Taniuchi[1,3], Kenichiro Hashimoto[1,7] & Takasada Shibauchi[1] ✉

Kagome metals host a variety of correlated electronic states, yet the nature of their intertwined orders remains an open question. The recently discovered Cr-based kagome compound $CsCr_3Sb_5$ differs from its V-based analogue CsV_3Sb_5 by exhibiting stronger correlations and a magnetic ground state. While multiple broken symmetries have been reported in CsV_3Sb_5, only a single transition at $T^* \approx 55$ K has been identified at ambient pressure in $CsCr_3Sb_5$, with its origin unresolved. Here we uncover an additional phase transition above T^* through elastoresistivity measurements. Rotational symmetry breaking without divergent nematic susceptibility is identified around $T \approx 64$ K, which is most consistently explained as the emergence of charge-density-wave order. Laser-based photoemission-electron microscopy further reveals three-domain structures associated with spin-density-wave order below T^*. These findings indicate distinct charge and spin order transitions in $CsCr_3Sb_5$, offering crucial insight into the intertwined orders and pressure-induced superconductivity in this system.

Kagome lattice has been a fascinating playground for condensed matter physics, due to its frustrating geometry and unique electronic structure hosting Dirac cones, van Hove singularities (vHSs), and flat bands[1,2]. Among many kagome materials, the AV_3Sb_5 (A = K, Rb, Cs) family has been a focus of extensive research since its recent discovery[3–23]. The nonmagnetic AV_3Sb_5 intriguingly displays superconductivity, charge density wave (CDW), electronic nematicity, and possible time-reversal symmetry breaking (TRSB)[7–14]. In this system hosting a layered kagome network of V atoms, the nesting between the vHSs just below the Fermi level E_F near the M points in the Brillouin zone (BZ) is believed to play a crucial role in realizing the exotic properties[18,19].

More recently, Cr-based kagome material $CsCr_3Sb_5$, which is isostructural to AV_3Sb_5, has emerged as a new playground. In contrast to the V-based AV_3Sb_5 featuring vHSs close to E_F, theoretical calculations predict Cr-3d-originated flat bands slightly above E_F[24–27]. Interestingly, several angle-resolved photoemission spectroscopy (ARPES) measurements report the existence of incipient flat bands 60–80 meV below E_F, indicating the strongly correlated nature of the system[28–30]. Strong electron correlations in $CsCr_3Sb_5$ are also witnessed by the enhanced Sommerfeld constant of 105 $mJK^{-2}mol^{-1}$, four times larger than that of CsV_3Sb_5[24]. Recent experimental results suggest intriguing coexistence of charge and magnetic orders in $CsCr_3Sb_5$[24,31]. The resistivity and heat capacity measurements resolved a single phase transi-

[1]Department of Advanced Materials Science, The University of Tokyo, Kashiwa, Chiba, Japan. [2]The Institute for Solid State Physics (ISSP), The University of Tokyo, Kashiwa, Chiba, Japan. [3]Material Innovation Research Center (MIRC), The University of Tokyo, Kashiwa, Chiba, Japan. [4]Department of Physics and Astronomy, Rice University, Houston, TX, USA. [5]Rice Laboratory for Emergent Magnetic Materials and Smally-Curl Institute, Rice University, Houston, TX, USA. [6]Department of Physics, Nagoya University, Nagoya, Japan. [7]Present address: Department of Physics, Kyoto University, Kyoto, Japan. [8]Present address: Department of Applied Physics, The University of Tokyo, Tokyo, Japan. ✉e-mail: onishi.a.lab@gmail.com; shibauchi@k.u-tokyo.ac.jp

tion at $T^* \approx 55$ K, and magnetic susceptibility and nuclear magnetic resonance (NMR) measurements indicated antiferromagnetic (AFM) order emerging below T^*[24]. Additionally, X-ray diffraction (XRD) measurements detected a 4×1 modulation within the kagome plane in the low-temperature phase, implying a CDW order and hexagonal to monoclinic structural transition[24,29]. However, the superstructure correlation is rather short-ranged and the electron-phonon coupling is weak, suggesting unconventional nature of the CDW[31]. Resistivity measurements under hydrostatic pressure suggest that the single transition at T^* changes into double transitions above around 2 GPa, and both transition temperatures decrease as the pressure increases. The suppression of transition temperatures continues to an emerging superconducting phase with optimal transition temperature $T_c = 6.4$ K at 4.2 GPa[24]. This may support the theoretical prediction of spin-fluctuation-mediated superconductivity in kagome systems with an incipient flat band[32].

While the V-based AV_3Sb_5 similarly hosts a CDW state, the unidirectional nature of the suggested $4 \times 1 \times 1$ CDW in $CsCr_3Sb_5$ contrasts with AV_3Sb_5, which exhibits $2 \times 2 \times 2$ or $2 \times 2 \times 4$ CDW modulations. Although such 2×2 modulations in AV_3Sb_5 are isotropic regarding the a-b plane, several experiments have reported rotational symmetry breaking in the system, giving rise to unsettled debates. Several experiments, such as magneto-resistivity, scanning tunnel microscopy (STM), and optical measurements, report rotational symmetry breaking with an onset that coincides with T_{CDW} or a lower temperature[8,12,33–35]. On the other hand, a few experiments[14,20,21], including magnetic torque measurements, suggest rotational symmetry breaking or a signature related to CDW far above T_{CDW}, indicating exotic CDW or electronic nematicity possibly arising from theoretically predicted charge-loop currents[22,23].

Such a rotational-symmetry-breaking feature is often related to electronic nematicity, where the electronic states spontaneously break rotational symmetry while preserving translational symmetry. Electronic nematicity has been found to be ubiquitous in strongly correlated electron systems including Fe-based superconductors (Fe-SCs), where nematicity originates from a spontaneous lifting of Fe-$3d_{xz}/d_{yz}$ orbitals, mostly coexisting with stripe-type spin density wave (SDW)[36–41].

In $CsCr_3Sb_5$, the suggested 4×1 CDW itself breaks the rotational symmetry of the original kagome lattice, contrasting to the case of AV_3Sb_5. In this regard, spontaneous rotational symmetry breaking or electronic nematicity provides a crucial key to understanding the interplay of multiple exotic orders. Although previous XRD and optical measurements suggested density-wave states, direct investigation of the breaking of rotational symmetry is mostly lacking[24,31,42].

Here, we use a powerful combination of linear dichroic (LD) measurements using a laser-based photoemission-electron microscopy (laser-PEEM) and bulk elastoresistivity measurements to investigate the rotational-symmetry-breaking orders in $CsCr_3Sb_5$. Laser-PEEM is a direct probe of the electronic states near $\bar{\Gamma}$, while elastoresistivity measurements are very sensitive to the rotational symmetry breaking of the system. We succeed in direct observations of three-domain structures associated with the SDW order, below $T_{SDW} = T^* \approx 55$ K. Moreover, we uncover another transition above T^* from the elastoresistivity measurements. We clearly resolve a kink in the elastoresistivity coefficients, together with the emergence of resistivity anisotropy and a signature of domain formation under strain at the same temperature. These results without divergent nematic susceptibility consistently identify the onset of CDW order at $T_{CDW} \approx 64$ K. A combination of those findings strongly suggests that density-wave orders with distinct transition temperatures successively emerge in $CsCr_3Sb_5$ at ambient pressure, and implies that different bands near BZ center and edges are responsible for the SDW and CDW orders in this system.

Results

Laser-PEEM imaging

To investigate the rotational-symmetry-breaking feature in $CsCr_3Sb_5$, we performed a powerful technique that directly visualizes anisotropy in electronic structures: laser-PEEM[38,43,44]. PEEM images map the spatial distribution of excited photoelectrons (Fig. 1a). One can obtain LD images representing anisotropy in electronic structures by using linearly polarized lights characterized by two polarization vectors perpendicular to each other: $\mathbf{E}_1$ and $\mathbf{E}_2$[38,44]. As illustrated in Fig. 1b, we define θ as the angle between $\mathbf{E}_1$ and the sample a axis. We obtain a real space mapping of PEEM intensity I_1 (I_2) using $\mathbf{E}_1$ ($\mathbf{E}_2$) polarization. The observable region in the energy-momentum space is limited depending on the energy of the incident light and work function of the surface (Fig. 1c, d). We use a continuous wave laser with energy $h\nu = 4.66$ eV, which is comparable to the work function ϕ of typical metals. We determined the maximum depth of the observable binding energy to be $\phi - h\nu = E - E_F \sim -1.1$ eV in our experiments (see Supplementary Information Sec. I). As the energy restriction also limits the observable size of wavevector $\mathbf{k}$, laser-PEEM captures electronic features of conductive electrons close to E_F around the $\bar{\Gamma}$ point of BZ.

Figure 2a–c show the mappings of LD asymmetry $I_{LD} = (I_1 - I_2)/I_0$ measured at 45 K with different polarization angles θ, where I_0 is the θ-independent component obtained from averaging over the all I_1 and I_2 images measured at $\theta = 0^\circ, 10^\circ, \ldots, 170^\circ$. Each image shows clear domain-like structures with different distributions depending on θ. Figure 2d shows the θ-dependence of LD intensity at three representative positions indicated in Fig. 2a. The LD intensity evidently shows oscillation depending on θ with the period of 180°, which indicates two-fold rotational symmetry, with different offsets of θ at each real space position. Therefore, we fit the θ-dependence of LD using

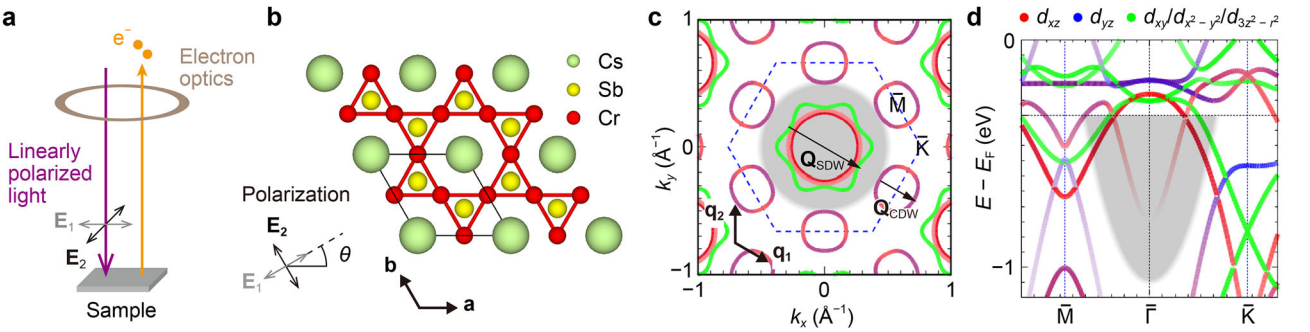

Fig. 1 | LD measurements in $CsCr_3Sb_5$ using laser-PEEM. a Schematics of LD measurements by using linearly polarized light with orthogonal configurations $\mathbf{E}_1$ and $\mathbf{E}_2$. **b** Kagome lattice of $CsCr_3Sb_5$ drawn by using VESTA[51] and the geometry between the light polarization and the sample. We define the polarization angle θ as the angle between the polarization vector $\mathbf{E}_1$ and the sample a axis. **c**, **d** The observable energy-momentum region in PEEM measurements using a 4.66 eV laser (shaded area), superimposed by the schematic electronic bands in $CsCr_3Sb_5$ (see Methods) with suggested SDW and CDW nesting vectors ($\mathbf{Q}_{SDW}$ and $\mathbf{Q}_{CDW}$, respectively). $\mathbf{q}_1$ and $\mathbf{q}_2$ denote reciprocal lattice vectors.

https://doi.org/10.1038/s41467-026-74096-8

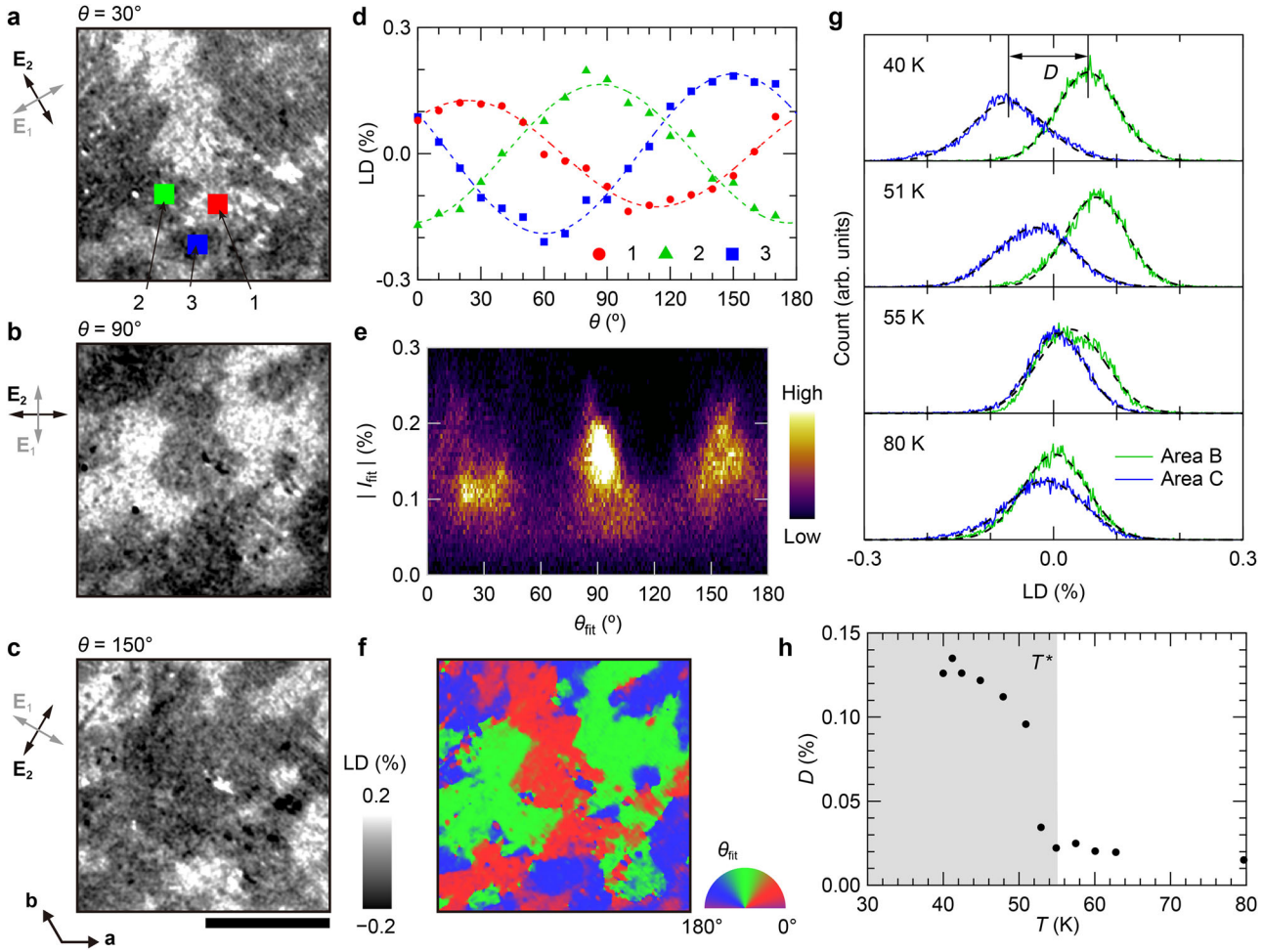

Fig. 2 | LD images of three-domain structures in $CsCr_3Sb_5$. LD images $I_{LD} = (I_1 - I_2)/I_0$ obtained at 45 K for $\theta = 30^\circ$ (**a**), 90° (**b**), and 150° (**c**). The black bar indicates 10 μm. **d**, The dependence of LD intensity on polarization angle θ at representative positions (1, 2, and 3 as indicated in **a**). The dashed lines represent fitting obtained using $I_{LD} = |I_{fit}| \cos 2(\theta - \theta_{fit})$. **e** Distributions of the fitting parameters $|I_{fit}|$ and θ_{fit}, obtained by fitting the θ dependence of LD at each pixel to $I_{LD} = |I_{fit}| \cos 2(\theta - \theta_{fit})$. **f** Spatial mapping of θ_{fit} at the same field of view as in (**a**–**c**). **g** Temperature dependence of the distribution of the LD intensity in areas B and C, where $\theta_{fit} = (90 \pm 30)^\circ$ and $(150 \pm 30)^\circ$, respectively. The dashed lines represent Gaussian fitting. **h** Temperature dependence of the LD contrast extracted from the difference D of peak positions of the two-Gaussian fitting in (**g**).

$I_{LD} = |I_{fit}| \cos 2(\theta - \theta_{fit})$ at every pixel captured in the LD images. The distribution of fitted parameters $|I_{fit}|$ and θ_{fit} shown in Fig. 2e indicates that the θ dependence of LD at each position is divided into three groups. Each group is characterized by different value of θ_{fit} ~ 30°, 90°, and 150°, while the intensity is similar ($|I_{fit}|$ ~ 0.1 to 0.2%). Such three different groups showing anisotropic LD at every 60° coincide with the emergence of three-state domains expected from the breaking of in-plane rotational symmetry from hexagonal six-fold to two-fold. The real space distribution of θ_{fit} shown in Fig. 2f clearly visualizes the structure of domains characterized by θ = 30°, 90°, and 150°, with a typical size of 5–10 μm, which is consistent with a rough estimate of ~ 10 μm from the spot size in the previous optical reflectivity measurements[42]. The three angles $\theta = 30^\circ$, 90°, and 150° correspond to three equivalent high symmetry directions (ignoring the difference of 180°) which are 90° respectively from the a and its equivalent axes.

We find that the contrast in intensity in images decreases by increasing the temperature (see Supplementary information Sec. II). To extract detailed temperature dependence, we grouped the image pixels into areas A, B, and C, where $\theta_{fit} = (30 \pm 30)^\circ$, $(90 \pm 30)^\circ$, and $(150 \pm 30)^\circ$, respectively. Figure 2g shows the distribution of LD intensity in areas B and C, obtained at $\theta = 70^\circ$. The center of each Gaussian-like distribution is separated from each other at low temperatures, and they match at high temperatures, reflecting the decrease of the LD contrast. We can evaluate this feature by defining the distance between the Gaussian centers as D, which is shown in Fig. 2g. Figure 2h represents the temperature dependence of D, a measure of LD contrast. This result reveals that LD in laser-PEEM becomes finite only below ≈ 55 K, which coincides nicely with the previously indicated transition temperature T^*.

Among Cr-3d and Sb-p_z orbitals, which are suggested to be present close to E_F by band calculations, only d_{xz} and d_{yz} contribute to LD signals, considering the orbital symmetry (see Supplementary Information Sec. III and IV). Across the transition at T^*, one of three energetically degenerated Cr-sites (Supplementary Fig. S3b) in the hexagonal phase is expected to become nonequivalent to the others. If we assume that the contribution from d_{yz} is small in the observable region in our laser-PEEM, as suggested from the band calculations (Fig. 1c, d), a decrease of d_{xz}-like density of states at one Cr-site compared to the others explains the θ-dependence of LD signals in each domain, where I_{LD} shows maximum values at $\theta = 30^\circ$, 90°, and 150°. On the other hand, previous ARPES measurements[28–30] report flat bands contributed from both d_{xz} and d_{yz} below E_F, although theoretical calculations predict flat bands lying above E_F. In parallel to the discussion above on d_{xz}, an increase of d_{yz}-like density of states at one Cr-site can

also explain the observed θ-dependence of LD signals. Note that either a band degeneracy lifting or a difference in spectral renormalization between the three Cr-sites can lead to the imbalance described above. The previous ARPES could not reveal such change in the band structure across the transition, due to a large beam spot size which does not allow to probe a single domain. The heavy band renormalization also makes it difficult to resolve the detailled band structure by ARPES and further investigations will be needed to distinguish which contribution is dominant. We note that the emergence of a unidirectional SDW order with $\mathbf{Q}_{\mathrm{SDW}} \approx (1/2, 0, 0)$ described in the following can induce distinct magnetic modulation at the three Cr-sites.

Elastoresistivity measurements

Having observed the three-domain structures below T^*, we next perform elastoresistivity measurements of $CsCr_3Sb_5$ to investigate resistivity responses under anisotropic strain. The anisotropic E_{2g} component of elastoresistivity coefficients serves as the nematic susceptibility, while the isotropic A_{1g} component captures various types of transitions. A square-like shaped single crystal was glued on the side of a piezostack to introduce anisotropic strain by applying an external voltage to the stack (Fig. 3a). We denote the strain polling direction as x. y axis is perpendicular to x and is along the a axis of the sample. Considering the hexagonal symmetry of the crystal, the system experiences a combination of isotropic A_{1g} strain $\frac{1}{2}(\epsilon_{xx}+\epsilon_{yy})$ and anisotropic E_{2g} strain $\frac{1}{2}(\epsilon_{xx}-\epsilon_{yy})$. The response of the electronic system to the applied strain can be evaluated by measuring the relative change in resistance $(\Delta\rho/\rho)_{ii}$. We used the modified Montgomery technique to measure both ρ_{xx} and ρ_{yy} at the same time and obtained the response in the A_{1g} and E_{2g} channels, $\frac{1}{2}(\Delta\rho_{xx}+\Delta\rho_{yy})/\rho_0$ and $\frac{1}{2}(\Delta\rho_{xx}-\Delta\rho_{yy})/\rho_0$, respectively[45]. Figure 3b, c show the dependence of resistivity on the strain in the A_{1g} and E_{2g} channels, respectively. Although we must note that the difference in thermal expansion coefficients between the sample and piezostack gives offset strain, which is not measurable by the strain gauge, we can sufficiently assume the overall resistivity response is in the linear regime. We can obtain the $A_{1g}(E_{2g})$ elastoresistivity coefficient $m_{A_{1g}}(m_{E_{2g}})$ as follows (see Supplementary Information Sec. V), by assuming the linearity in data in Fig. 3b, c, and by fitting the slope of the curve at each temperature:

$$m_{A_{1g}} = \frac{\frac{1}{2}[(\Delta\rho/\rho)_{xx}+(\Delta\rho/\rho)_{yy}]}{\frac{1}{2}(\epsilon_{xx}+\epsilon_{yy})}, \quad (1)$$

$$m_{E_{2g}} = \frac{\frac{1}{2}[(\Delta\rho/\rho)_{xx}-(\Delta\rho/\rho)_{yy}]}{\frac{1}{2}(\epsilon_{xx}-\epsilon_{yy})}. \quad (2)$$

Figure 3d shows the temperature dependence of elastoresistivity coefficients $m_{A_{1g}}$ and $m_{E_{2g}}$. In the case of Fe-SCs, the anisotropic $m_{B_{2g}}$ elastoresistivity coefficient captures the nematic fluctuation above the transition temperature and diverges in the Curie-Weiss form $\propto \frac{1}{T-\Theta}$ towards Θ, serving as nematic susceptibility which provides a benchmark signature of the $\mathbf{q} = 0$ ferro-nematic transition[40,46]. On the other hand, in AV_3Sb_5, any temperature dependence in anisotropic $m_{E_{2g}}$ is absent above T_{CDW} while various other techniques report the breaking of rotational symmetry, indicating a more complex nature of nematicity in the V-based kagome metals[14–16].

The temperature dependence of the anisotropic elastoresistivity coefficient $m_{E_{2g}}$ in $CsCr_3Sb_5$ is in stark contrast to both Fe-SCs and AV_3Sb_5 cases. As the temperature decreases, $m_{E_{2g}}$ starts to increase below the onset temperature at ≈ 64 K, while it shows only slight temperature dependence above. Such temperature dependence deviates from the Curie-Weiss divergence observed in Fe-SCs, suggesting that the conventional $\mathbf{q} = 0$ ferro-nematic instability of Fe-SC type is unlikely in this material. However, we note that the absence of a Curie-Weiss form alone does not strictly exclude the possibility of electronic nematicity and the enhancement of $m_{E_{2g}}$ below ≈ 64 K may also be interpreted in terms of nematic fluctuations, as we discuss later. Besides, the unexpected increase from ~ 9 K above T^* indicates the existence of a change in the electronic structure well above the known transition temperature $T^* \approx 55$ K. Additionally, the isotropic elastoresistivity coefficient $m_{A_{1g}}$ shows a sudden drop below the same temperature ≈ 64 K, indicating a clear sign of the change in the electronic state. It is worth noting that similar anomalies in the elastoresistivity coefficients are found in incommensurate-CDW and nematic phase of the Ni-based counterpart of Fe-SCs, $BaNi_2As_2$ family, which precedes concurrent structural and commensurate-CDW transition[47,48].

To get further insight into the intriguing physical properties above T^*, we compare the resistivity along x and y directions. Figure 3e shows the temperature dependence of ρ_{xx} and ρ_{yy} under offset strain described above. One can see that the two signals deviate from each other below ≈ 64 K. We can obtain the anisotropy of the two signals by calculating $(\rho_{yy}-\rho_{xx})/(\rho_{yy}+\rho_{xx})$ shown in Fig. 3e. The resistive anisotropy onsets at ≈ 64 K and develops towards T^* as a second-order transition, which clearly indicates its rotational symmetry breaking nature. The kink in the elastoresistivity coefficients (related to the slope in the resistivity-strain curves) and the onset of the resistivity anisotropy occur at the same temperature, which implies that this signature of transition is not strain induced. Indeed, a careful look into the previously reported resistivity data[24,28,42] may resolve subtle anomalies at around 64 K. In addition, the NMR spectra show some slight broadening below ~ 67 K well above T^*[24]. It is presumably due to a weak splitting of the potential at the Sb sites introduced by the translational symmetry breaking CDW. Thus, it is most likely that the application of anisotropic strain can induce imbalance of domains, which leads to the observation of resistive anisotropy below the transition present even without strain. We also note that the CDW transition temperature in CsV_3Sb_5 is shifted only by ~0.1% with $\epsilon_{xx} = 10^{-4}$[14].

The domain formation due to rotational symmetry breaking can also be studied by the hysteresis behavior in the ρ versus strain curves, which is indeed observed in some data in Fig. 3b, c. To explore this further, we employ another elastoresistivity technique using the four-terminal resistivity measurements with a bar-like shaped crystal. Figure 3f shows the schematic of the setup and the response in resistivity under sweeping strain at a representative temperature. The curves under increasing and decreasing strain clearly show the hysteresis behavior. Figure 3g shows a temperature dependence of the hysteresis size, which is defined as the area inside the loop (shaded part in Fig. 3f) divided by the range of the sweeping strain for normalization. The size of the hysteresis becomes finite and develops below the same temperature ≈ 64 K as the onset of resistive anisotropy. This feature strongly indicates the breaking of symmetry because the finite hysteresis in the elastoresistivity loop is reasonably attributed to the change of the ratio of domains, whose existence cannot be explained by isotropic translational-symmetry breaking like 2×2 CDW in AV_3Sb_5 but by rotational symmetry breaking. We note that similar hysteresis behaviors in elastoresistivity have also been observed in materials that host rotational symmetry breaking CDW orders: $BaNi_2As_2$ family and RTe_3 (R = Er, Tm)[47–49]. The right axis of Fig. 3g represents the temperature dependence of the slope of elastoresistivity loops $d(\Delta\rho_{xx}/\rho_{xx})/d\epsilon_{xx}$ using the bar-shaped sample. Although the four-probe method with a single sample does not resolve the symmetric components, $d(\Delta\rho_{xx}/\rho_{xx})/d\epsilon_{xx}$ under anisotropic biaxial strain is expected to be dominated by $m_{E_{2g}}$ contaminated with $m_{A_{1g}}$. The increase of the signal below ≈ 64 K confirms that this behavior is the intrinsic nature of $CsCr_3Sb_5$ and not sample-dependent.

These three independent measurements—namely, the elastoresistivity coefficients, resistive anisotropy, and the domain formation—

https://doi.org/10.1038/s41467-026-74096-8

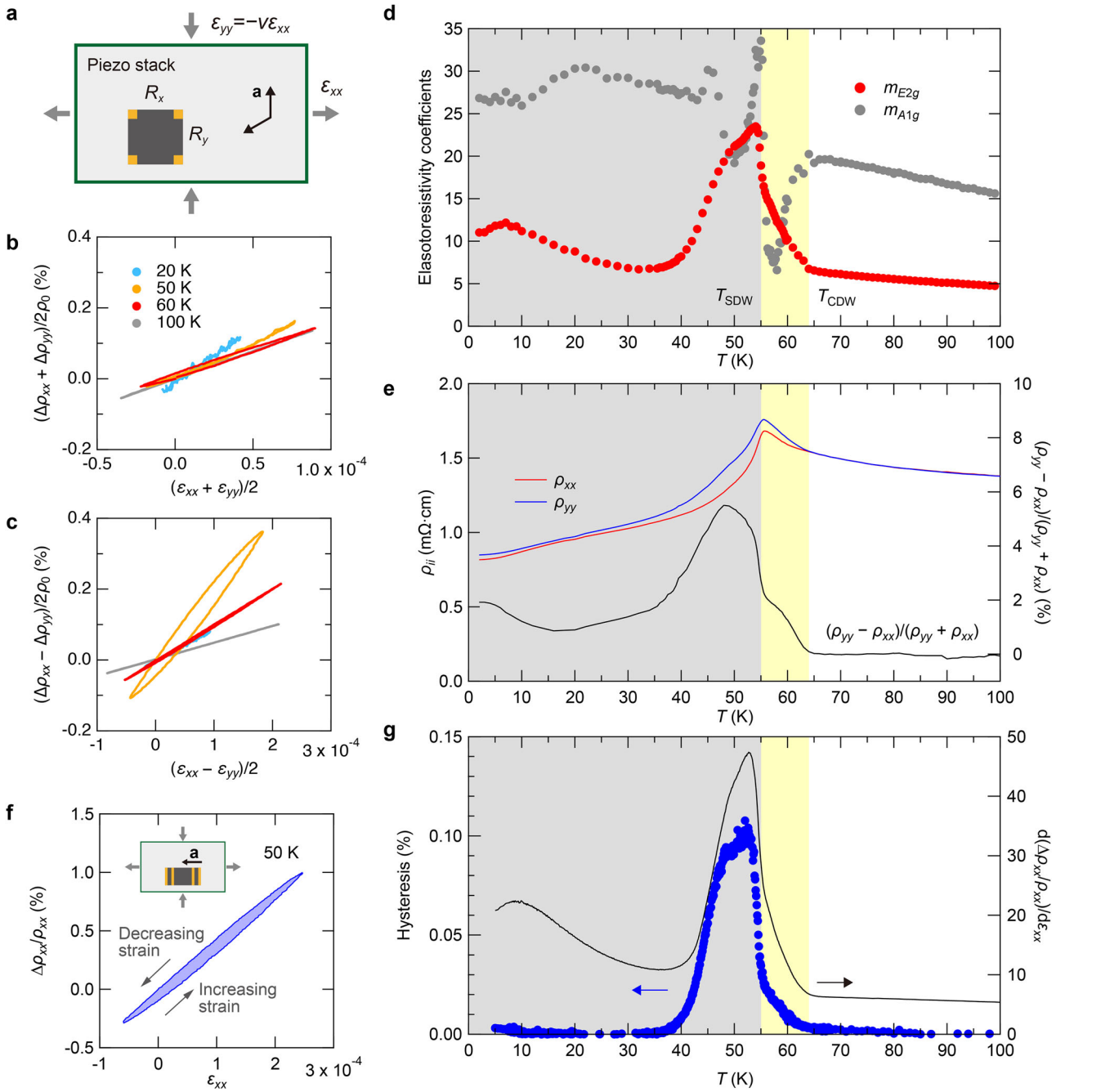

Fig. 3 | Elastoresistivity measurements in $CsCr_3Sb_5$. a, Schematics of elastoresistivity measurements. The sample is glued on the side of a piezostack. Sample resistivity is measured using the modified Montgomery technique. The *a* axis of the sample is perpendicular to the polling direction of the piezostack. Relative changes in the resistivity as a function of strain in the isotropic A_{1g} (**b**) and the anisotropic E_{2g} (**c**) channels measured at various temperatures. **d** Temperature dependence of elastoresistivity coefficients. **e** Temperature dependence of ρ_{xx} (red), ρ_{yy} (blue), and anisotropy between them (black) measured under offset strain by the modified Montgomery configuration. **f** Representative data of the change in resistivity under strain using a bar-shaped crystal. The blue shaded area inside the loop plot represents the size of the hysteresis in the resistivity change under increasing and decreasing strain. The inset shows the schematic of elastoresistivity measurements using the four-terminal method with a bar-shaped crystal, where the *a* axis is parallel to the polling direction of the piezostack. **g** Temperature dependence of the hysteresis area (blue points) and slope of elastoresistivity loops (black line).

consistently indicate the existence of a second-order transition with rotational symmetry breaking at ≈ 64 K distinctly separated from $T^* \approx 55$ K. Importantly, the absence of a divergence in $m_{E_{2g}}$ rules out the conventional (even-parity) type of $\mathbf{q} = 0$ electronic nematicity from the candidates. Besides, the absence of laser-PEEM LD signal above T^* shows that the transition at ≈ 64 K gives little change to the symmetry of electronic structure around $\bar{\Gamma}$ (see Fig. 1c). As the previous magnetic susceptibility measurement shows a single anomaly at T^*, it is natural to assign T^* as the magnetic SDW transition T_{SDW}, while the new one at ≈ 64 K is a nonmagnetic charge order transition.

Discussion

From these results, we propose that a CDW order emerges at $T_{CDW} \approx 64$ K, preceding the magnetic phase transition at $T_{SDW} \approx 55$ K. It

should be noted that, the synchrotron X-ray measurements reported that the 4 × 1 superlattice structure is resolved but its underlying correlation is rather short ranged[31], and the weak electron-phonon coupling may make the unconventional CDW transition difficult to observe from the structural studies. Indeed, a recent theoretical study based on first-principles calculations points out that the CDW and SDW instabilities are associated with distinctly different band nesting behaviors (Y. Yamakawa and H. Kontani, in preparation). An intraband nesting with $\mathbf{Q}_{\mathrm{CDW}} \approx (1/4, 0, 0)$ in the electron pocket around the M point (near the BZ edges) gives rise to 4 × 1 CDW, while another nesting with $\mathbf{Q}_{\mathrm{SDW}} \approx (1/2, 0, 0)$ contributed from the two hole and one electron pockets around the Γ point induces 2 × 1 SDW (Fig. 1c). As the observable range of our laser-PEEM measurements in the E-k space is limited around the $\bar{\Gamma}$ point (Fig. 1c, d), this can fully explain that the LD signals only reflect the SDW transition involving the bands around the Γ point and are insensitive to the CDW transition involving the electron pocket around the M point. The second-order nature of the CDW transition at $T_{\mathrm{CDW}} \approx 64$ K found here, which is associated from the small pocket near M point, may also suppress the specific heat anomaly compared with the SDW transition at T^*, which may be masked by the large lattice contribution to the heat capacity in such a high temperature range. Finally, the successive double transitions observed in the resistivity measurements under pressure can be naturally accounted for by this explanation that the SDW and CDW transition temperatures were different from the first place (see Supplementary information Sec. VI), rather than that they split under pressure[24].

It should also be noted, however, that the elastoresistivity data alone cannot uniquely determine the microscopic origin of the anomaly at ≈ 64 K. We therefore discuss the following alternative scenarios.

(i) Long-range rotational symmetry breaking order. The three independent observations—the kink in the temperature dependence of $m_{E_{2g}}$ and $m_{A_{1g}}$, the onset of resistivity anisotropy, and the hysteresis in strain–resistivity loops—are all consistent with a rotational-symmetry-breaking transition. Given that magnetic susceptibility shows an anomaly only at T^*, a charge-related order remains a plausible candidate. Temperature resolution of the existing XRD data do not strictly exclude a scenario in which a 4 × 1 CDW begins to develop near 64 K[24,31]. However, elastoresistivity alone cannot determine the modulation period, and possibilities such as incommensurate order or bond-density-wave order cannot be excluded.

(ii) Short-range order. A short-range CDW breaking rotational symmetry is another possibility. However, such a scenario would be more difficult to reconcile with the observed hysteresis, which naturally arises from strain-induced redistribution of symmetry-related domains in a long-range ordered phase.

(iii) Nematic fluctuation regime. The enhancement of $m_{E_{2g}}$ below 64 K and its further increase toward T^* may reflect nematic fluctuations towards a possible nematic transition at T^*, rather than a distinct phase transition at 64 K. Although the temperature dependence of $m_{E_{2g}}$ does not follow a Curie–Weiss form $\propto \frac{1}{T-\Theta}$, nematic fluctuations cannot be strictly excluded. In this scenario, the resistivity anisotropy $(\rho_{yy} - \rho_{xx})/(\rho_{yy} + \rho_{xx})$ could arise from the elastoresistive response to residual strain due to differential thermal contraction between the sample and the piezostack. However, this scenario is difficult to reconcile with a comparison between two samples in different crystallographic orientations relative to the piezo polling direction x (see Supplementary information Sec. VII): below 64 K, the temperature dependence of ρ_{xx} in the four-terminal sample (with $a \| x$) resembles that of ρ_{yy} in the modified Montgomery sample (with $a \| y$), rather than ρ_{xx}. Such behavior contrasts with an expectation that the elastoresistive response depends on the straining x–y frame regardless of crystal orientation, when the system is still above the rotational-symmetry-breaking transition.

(iv) Broadening of the T^* transition by residual strain. Residual strain due to differential thermal contraction between the sample and the piezostack is inevitably present in our measurements. If this broadened the 55 K transition up to around 64 K, one would expect the associated anomalies to become substantially smeared. In contrast, well-defined features such as a clear onset of anisotropy around 55 K in Fig. 3e are inconsistent with such broadening. Another possible effect from the residual strain may be that it shifted T^* by ~10 K. However, at such a strong sensitivity, one can expect that the sweeping of strain near 64 K would drive the system to cross the phase boundary during a single strain loop, producing a noticeable change in slope in the strain–resistivity curve. No such behavior is observed experimentally (see Supplementary information Sec. VIII). We therefore consider broadening of the 55 K transition to be an unlikely explanation for the 64 K anomaly.

We note that the hysteresis observed in Fig. 3b, c, f, and g provides the strongest constraint among our observations: it is naturally interpreted as arising from strain-induced changes in the population of symmetry-related domains, implying the existence of a symmetry-broken phase. While a fully conclusive assignment of the 64 K anomaly awaits additional measurements, our combined results most consistently point to a rotational-symmetry-breaking transition tentatively associated with CDW order.

We note that the emergence of a unidirectional SDW possibly explain the finite LD signals below T^* in the laser-PEEM measurements. While the specific pattern of spins in the 2 × 1 SDW state is still unknown, the unidirectional SDW induces distinct magnetic modulations at each Cr-site. For example, a simple stripe-type AFM configuration (Supplementary Fig. S3c) induces magnetic moment at two out of three Cr-sites, leaving one site neutral. In spite that little change is observed in the metallic band structure across the SDW transition in the previous ARPES[28–30], except for a slight (~20 meV) downward shift of the reported flat bands[29] and a reduction of FWHM at the Sb-p-like band near E_{F}[28], the resistivity drastically changes from semiconducting-like to metallic across T_{SDW} (Fig. 3e). Such features indicate strong scattering of electrons near E_{F} in the normal state and that the emergence of SDW recovers their coherence and thus the spectral weight. In that sense, imbalance in the magnetic moments at each site or consequent unidirectional band folding and anisotropic gap opening possibly give inequivalent spectral weights between the bands each related to the distinct Cr-site. Because the exact implementation behind the LD might be more complex depending on the specific pattern of spins, the detail of the band structure, and its change across the transition, further theoretical and experimental studies including neutron scattering measurements are needed to reveal the detailed relation between the SDW and LD.

Finally, we note that a non-monotonic feature is observed in $m_{E_{2g}}$ and $(\rho_{yy} - \rho_{xx})/(\rho_{yy} + \rho_{xx})$ below approximately 10 K in both samples measured with different configurations. The reproducibility across samples and measurement geometries imply that this feature is intrinsic and not a measurement artifact. Its origin remains unclear at present and appears distinct from the CDW and SDW transitions discussed above; this low-temperature feature may provide an interesting direction for future investigations.

To summarize, the unique combination of laser-PEEM sensitive to electronic states near $\bar{\Gamma}$ and the elastoresistivity measurements enables us to distinguish the CDW and SDW orders with distinct transition temperatures originating from different band nesting properties. Our findings highlight the complex nature of electronic orders emerging in $CsCr_3Sb_5$ and provide a clue to disentangle the intertwined orders. In addition, they offer important information on understanding the electronic phase diagrams of correlated kagome metals including the pressure-induced superconductivity associated with the fate of density wave orders.

Methods

Crystal growth and characterization

Single crystal samples of $CsCr_3Sb_5$ were grown by the self-flux method. Detailed methods are described in ref. 29. We obtained flat (along the hexagonal *a*-*b* plane) and thin (typical thickness along the *c*-axis of < 5 μm) crystalline flakes. Typical sample dimensions used in laser-PEEM and elastoresistivity measurements were $\lesssim$500 μm square along the *a*-*b* plane. Axis directions were characterized by X-ray diffraction for each sample after elastoresistivity and laser-PEEM measurements.

The residual resistivity ratio $R_{100\,K}/R_{0\,K}$ is approximately 2.3 for both samples used in the elastoresistivity measurements (modified Montgomery and four-terminal configurations), indicating comparable sample quality. This value is comparable to or slightly higher than that reported in prior work[24], where $R_{100\,K}/R_{0\,K} \approx 1.7$ was reported, suggesting that disorder effects are unlikely to qualitatively alter the observed behavior.

Laser-PEEM measurements

We used laser-PEEM at the Institute for Solid State Physics (ISSP), the University of Tokyo, to obtain LD images. The light source is a continuous-wave laser of 4.66 eV (λ = 266 nm)[38,43,44]. The light incident was normal to the sample surface (*ab*-plane). A half-wave plate controlled the polarization angle θ of the linearly polarized light and PEEM image I_1 was obtained at $\theta = 0^\circ, 10^\circ, \ldots, 170^\circ$. Corresponding image I_2 with $\theta + 90^\circ$ was obtained by switching a Pockels cell on, at each $\theta = 0^\circ, 10^\circ, \ldots, 170^\circ$. The θ-independent image I_0 for normalization of LD ($I_{LD} = (I_1 - I_2)/I_0$) was obtained by averaging all I_1 and I_2 images. A flat single crystal was glued on the sample holder using a conducting epoxy (EPO-TEK, H20E) with a cleaving post. The sample was cleaved in ultra-high vacuum (base pressure $< 6 \times 10^{-10}$ Torr) at room temperature and then transferred to another ultra-high vacuum low-temperature measurement setup, where the base pressure was better than 2×10^{-10} Torr.

Elastoresistivity measurements

As the single-crystal samples were thin and fragile (typical thickness along the *c*-axis is < 5 μm), we used as-grown samples with square-like and bar-like shapes, in the measurements using the modified Montgomery and four-terminal techniques, respectively.

Single crystals were glued (using an epoxy Araldite RT30) on the side of a piezoelectric device (Piezomechanik PSt 150/3.5 × 3.5/7). The amount of strain ϵ_{xx} along the polling direction x was controlled by applying the voltage to the piezoelectric device and monitored by a strain gauge (CFLA-1-350-11, TML) attached to the other side of the device. The strain along the orthogonal direction y was calculated using Poisson's ratio of the piezostack calibrated beforehand. By assuming that the response of ρ_{ii} versus strain is in the linear regime and thus that the offset strain is sufficiently small, we set the zero-point of strain to be the values where the voltage applied to the piezostack is zero. Note that the applied voltage was swept asymmetrically from − 30 V to 150 V in the measurements, reflecting the compliance characteristics of the piezoelectric device. As a result, the strain–resistivity hysteresis loops are not centered around zero strain.

In the modified Montgomery technique[45,50], we made electric contacts at the four corners of a square-shaped sample. The *a* axis of the sample was aligned along the y axis, which is perpendicular to the polling direction x of the piezoelectric device. The resistance R_x (R_y) along the x (y) direction was measured by sourcing current between the pair of contacts at the corner of a sample edge along the x (y) direction, and measuring the voltage between the contacts on the other side. ρ_{xx} and ρ_{yy} were obtained using R_x and R_y via the following equations[45]:

$$\rho_{xx} = \frac{8}{\pi}\left(\frac{L_z L_y}{L_x}\right)\left(\frac{L_x'}{L_y'}\right) R_x \sinh\left(\frac{\pi L_y'}{L_x'}\right), \tag{3}$$

$$\rho_{yy} = \frac{8}{\pi}\left(\frac{L_z L_x}{L_y}\right)\left(\frac{L_y'}{L_x'}\right) R_y \sinh\left(\frac{\pi L_x'}{L_y'}\right), \tag{4}$$

$$\frac{L_y'}{L_x'} \approx \frac{1}{2}\left[\frac{1}{\pi}\ln\frac{R_y}{R_x} + \sqrt{\left(\frac{1}{\pi}\ln\frac{R_y}{R_x}\right)^2 + 4}\right], \tag{5}$$

where L_x (L_y) is the sample length along the x (y) direction.

In the four-terminal technique, the *a* axis of a bar-shaped sample was aligned along the polling direction x of the piezoelectric device. Resistivity ρ_{xx} along the x direction was measured using the standard four-terminal resistance measurement technique.

DFT calculations

First-principles calculations for $CsCr_3Sb_5$ were carried out using the WIEN2k code within the framework of density functional theory (DFT), employing the full-potential linearized augmented plane wave (FP-LAPW) method. The generalized gradient approximation (GGA) in the Perdew-Burke-Ernzerhof (PBE) form was adopted for the exchange-correlation functional. The experimentally reported crystal structure from ref. 24 was directly used for all calculations, and no structural optimization was performed. Using the Wannier90 code, a 30-orbital tight-binding model was constructed via maximally localized Wannier function method, and the band structure and Fermi surface were obtained. The schematic electronic structures in Fig. 1c, d are calculated by the two-dimensional model, where the interlayer hopping is ignored. The Fermi-surface structure obtained in this model is close to the one for $k_z = \pi/2$ in the three-dimensional calculation.

Data availability

Source data are provided with this paper. All other data that support the plots within this paper are available from the corresponding authors upon request.

References

1. Syôzi, I. Statistics of Kagomé Lattice. *Prog. Theor. Phys.* **6**, 306–308 (1951).
2. Yin, J.-X., Lian, B. & Hasan, M. Z. Topological kagome magnets and superconductors. *Nature* **612**, 647–657 (2022).
3. Wilson, S. D. & Ortiz, B. R. AV_3Sb_5 kagome superconductors. *Nat. Rev. Mater.* **9**, 420–432 (2024).
4. Ortiz, B. R. et al. New kagome prototype materials: Discovery of KV_3Sb_5, RbV_3Sb_5, and CsV_3Sb_5. *Phys. Rev. Mater.* **3**, 094407 (2019).
5. Neupert, T., Denner, M. M., Yin, J.-X., Thomale, R. & Hasan, M. Z. Charge order and superconductivity in kagome materials. *Nat. Phys.* **18**, 137–143 (2022).
6. Ortiz, B. R. et al. CsV_3Sb_5: A $\mathbb{Z}_2$ Topological Kagome metal with a superconducting ground state. *Phys. Rev. Lett.* **125**, 247002 (2020).
7. Zhao, H. et al. Cascade of correlated electron states in the kagome superconductor CsV_3Sb_5. *Nature* **599**, 216–221 (2021).
8. Xiang, Y. et al. Twofold symmetry of c-axis resistivity in topological kagome superconductor CsV_3Sb_5 with in-plane rotating magnetic field. *Nat. Commun.* **12**, 6727 (2021).
9. Jiang, Y.-X. et al. Unconventional chiral charge order in kagome superconductor KV_3Sb_5. *Nat. Mater.* **20**, 1353–1357 (2021).
10. Mielke, C. et al. Time-reversal symmetry-breaking charge order in a kagome superconductor. *Nature* **602**, 245–250 (2022).
11. Khasanov, R. et al. Time-reversal symmetry broken by charge order in CsV_3Sb_5. *Phys. Rev. Res.* **4**, 023244 (2022).
12. Nie, L. et al. Charge-density-wave-driven electronic nematicity in a kagome superconductor. *Nature* **604**, 59–64 (2022).

13. Roppongi, M. et al. Bulk evidence of anisotropic *s*-wave pairing with no sign change in the kagome superconductor CsV_3Sb_5. *Nat. Commun.* **14**, 667 (2023).
14. Asaba, T. et al. Evidence for an odd-parity nematic phase above the charge-density-wave transition in a kagome metal. *Nat. Phys.* **20**, 40–46 (2024).
15. Frachet, M. et al. Colossal c-Axis response and lack of rotational symmetry breaking within the Kagome planes of the CsV_3Sb_5superconductor. *Phys. Rev. Lett.* **132**, 186001 (2024).
16. Liu, Z. et al. Absence of E_{2g} nematic instability and dominant A_{1g} response in the Kagome metal CsV_3Sb_5. *Phys. Rev. X.* **14**, 031015 (2024).
17. Sur, Y., Kim, K.-T., Kim, S. & Kim, K. H. Optimized superconductivity in the vicinity of a nematic quantum critical point in the kagome superconductor $Cs(V_{1-x}Ti_x)_3Sb_5$. *Nat. Commun.* **14**, 3899 (2023).
18. Tazai, R., Yamakawa, Y., Onari, S. & Kontani, H. Mechanism of exotic density-wave and beyond-Migdal unconventional superconductivity in kagome metal AV_3Sb_5 (A = K, Rb, Cs). *Sci. Adv.* **8**, eabl4108 (2022).
19. Kang, M. et al. Twofold van Hove singularity and origin of charge order in topological kagome superconductor CsV_3Sb_5. *Nat. Phys.* **18**, 301–308 (2022).
20. Chen, Q., Chen, D., Schnelle, W., Felser, C. & Gaulin, B. D. Charge density wave order and fluctuations above T_{CDW} and below Superconducting T_c in the Kagome metal CsV_3Sb_5. *Phys. Rev. Lett.* **129**, 056401 (2022).
21. Liu, H. et al. Fluctuated lattice-driven charge density wave far above the condensation temperature in kagome superconductor KV_3Sb_5. *Sci. Bull.* **70**, 1211–1214 (2025).
22. Tazai, R., Yamakawa, Y. & Kontani, H. Charge-loop current order and Z_3 nematicity mediated by bond order fluctuations in kagome metals. *Nat. Commun.* **14**, 7845 (2023).
23. Li, H., Kim, Y. B. & Kee, H.-Y. Intertwined Van Hove singularities as a mechanism for loop current order in Kagome Metals. *Phys. Rev. Lett.* **132**, 146501 (2024).
24. Liu, Y. et al. Superconductivity under pressure in a chromium-based kagome metal. *Nature* **632**, 1032–1037 (2024).
25. Xie, F. et al. Electron correlations in the kagome flat band metal $CsCr_3Sb_5$. *Phys. Rev. Res.* **7**, L022061 (2025).
26. Wang, Y. Heavy fermions in frustrated Hund's metal with portions of incipient flat bands. *Phys. Rev. B* **111**, 035127 (2025).
27. Wu, S. et al. Flat-band enhanced antiferromagnetic fluctuations and superconductivity in pressurized $CsCr_3Sb_5$. *Nat. Commun.* **16**, 1375 (2025).
28. Li, Y. et al. Electron correlation and incipient flat bands in the Kagome superconductor $CsCr_3Sb_5$. *Nat. Commun.* **16**, 3229 (2025).
29. Wang, Z. et al. Spin excitations and flat electronic bands in a Cr-based kagome superconductor. *Nat. Commun.* **16**, 7573 (2025).
30. Peng, S. et al. Flat bands and distinct density wave orders in correlated Kagome superconductor $CsCr_3Sb_5$. *Sci. China Phys., Mech. Astron.* **69**, 217412 (2025).
31. Yao, W. et al. Absence of acoustic phonon anomaly in a Kagome metal with short-ranged structural modulation. Preprint at https://doi.org/10.48550/arXiv.2410.16465 (2024).
32. Aida, T., Matsumoto, K., Ogura, D., Ochi, M. & Kuroki, K. Theoretical study of spin-fluctuation-mediated superconductivity in two-dimensional Hubbard models with an incipient flat band. *Phys. Rev. B* **110**, 054516 (2024).
33. Wu, Q. et al. Simultaneous formation of two-fold rotation symmetry with charge order in the kagome superconductor CsV_3Sb_5 by optical polarization rotation measurement. *Phys. Rev. B* **106**, 205109 (2022).
34. Xu, Y. et al. Three-state nematicity and magneto-optical Kerr effect in the charge density waves in kagome superconductors. *Nat. Phys.* **18**, 1470–1475 (2022).
35. Deng, Q. et al. Revealing rotational symmetry breaking charge density wave order in the kagome superconductor $(Rb, K)V_3Sb_5$ by ultrafast pump-probe experiments. *Phys. Rev. B* **111**, 165134 (2025).
36. Fernandes, R. M., Chubukov, A. V. & Schmalian, J. What drives nematic order in iron-based superconductors? *Nat. Phys.* **10**, 97–104 (2014).
37. Böhmer, A. E., Chu, J.-H., Lederer, S. & Yi, M. Nematicity and nematic fluctuations in iron-based superconductors. *Nat. Phys.* **18**, 1412–1419 (2022).
38. Shimojima, T. et al. Discovery of mesoscopic nematicity wave in iron-based superconductors. *Science* **373**, 1122–1125 (2021).
39. Shimojima, T. et al. Lifting of *xz*/*yz* orbital degeneracy at the structural transition in detwinned FeSe. *Phys. Rev. B* **90**, 121111 (2014).
40. Chu, J.-H., Kuo, H.-H., Analytis, J. G. & Fisher, I. R. Divergent nematic susceptibility in an iron arsenide superconductor. *Science* **337**, 710–712 (2012).
41. Hosoi, S. et al. Nematic quantum critical point without magnetism in $FeSe_{1-x}S_x$ superconductors. *Proc. Natl. Acad. Sci. USA.* **113**, 8139–8143 (2016).
42. Liu, L. et al. Unraveling intertwined orders in the strongly correlated kagome metal $CsCr_3Sb_5$. *Natl. Sci. Rev.* **13**, nwag044 (2026).
43. Taniuchi, T., Kotani, Y. & Shin, S. Ultrahigh-spatial-resolution chemical and magnetic imaging by laser-based photoemission electron microscopy. *Rev. Sci. Instrum.* **86**, 023701 (2015).
44. Kageyama, Y. et al. Coherence Length of Electronic Nematicity in Iron-Based Superconductors. *J. Phys. Soc. Jpn.* **93**, 103702 (2024).
45. dos Santos, C. A. M. et al. Procedure for measuring electrical resistivity of anisotropic materials: a revision of the Montgomery method. *J. Appl. Phys.* **110**, 083703 (2011).
46. Kuo, H.-H., Chu, J.-H., Palmstrom, J. C., Kivelson, S. A. & Fisher, I. R. Ubiquitous signatures of nematic quantum criticality in optimally doped Fe-based superconductors. *Science* **352**, 958–962 (2016).
47. Eckberg, C. et al. Sixfold enhancement of superconductivity in a tunable electronic nematic system. *Nat. Phys.* **16**, 346–350 (2020).
48. Frachet, M. et al. Elastoresistivity in the incommensurate charge density wave phase of $BaNi_2(As_{1-x}P_x)_2$. *npj Quantum Mater.* **7**, 115 (2022).
49. Straquadine, J. A. W., Ikeda, M. S. & Fisher, I. R. Evidence for realignment of the charge density wave state in $ErTe_3$ and $TmTe_3$ under uniaxial stress via elastocaloric and elastoresistivity measurements. *Phys. Rev. X.* **12**, 021046 (2022).
50. Montgomery, H. C. Method for measuring electrical resistivity of anisotropic materials. *J. Appl. Phys.* **42**, 2971–2975 (1971).
51. Momma, K. & Izumi, F. *VESTA3* for three-dimensional visualization of crystal, volumetric and morphology data. *J. Appl. Crystallogr.* **44**, 1272–1276 (2011).

Acknowledgements

We thank the fruitful discussions with Takahiro Shimojima and Supeng Liu. We appreciate Kozo Okazaki for arranging the laser-PEEM experiments under the Institute for Solid State Physics (ISSP) joint-research programs. Sample characterization by XRD at the University of Tokyo was performed using the facilities of the Materials Design and Characterization Laboratory in the ISSP, the University of Tokyo (No. 202406-MCBXG-0108).

Author contributions

K.H. and T.S. conceived the project. A.O., Y.K., S.I. and Z.X. performed elastoresistivity measurements and analyzed the data under the guidance of K.I., K.H. and T.S. A.O., Y.K. and C.B. carried out laser-PEEM measurements and analyzed the data with the help of H.F. under the guidance T.T. Single crystals were synthesized and characterized by Z.W. and B.G. under the guidance of P.D. Y.Y. and H.K. performed theoretical calculations. A.O., K.H. and T.S. prepared the manuscript with inputs from C.B., T.T., W.Y., P.D., Y.Y. and H.K. All authors discussed the experimental results.

Funding
This work was supported by a Grant-in-Aid for Transformative Research Areas (A) "Correlation Design Science" (No. JP25H01248), by Grants-in-Aid for Scientific Research (KAKENHI) (Nos. JP22H00105, JP25H00838, and JP26K21719) from Japan Society for the Promotion of Science, by Quantum Materials Accelnet supernetwork program from the Institute for Complex Adaptive Matter, and by JST SPRING (Grant No. JPMJSP2108). The single-crystal synthesis and characterization work at Rice were supported by the U.S. DOE, BES under Grant Nos. DE-SC0012311 and DE-SC0026179 (P.D.). Part of the materials characterization efforts at Rice is supported by the Robert A. Welch Foundation Grant No. C-1839 (P.D.).

Competing interests
The authors declare no competing interests.

Additional information
Supplementary information The online version contains supplementary material available at https://doi.org/10.1038/s41467-026-74096-8.

Correspondence and requests for materials should be addressed to Asato Onishi or Takasada Shibauchi.

Peer review information *Nature Communications* thanks Laurenz Rettig who co-reviewed with Mohamed WahadaSergio Ulloa and the other, anonymous, reviewer(s) for their contribution to the peer review of this work. A peer review file is available.